High-pressure inelastic neutron scattering study of the anisotropic S = 1 spin chain [Ni(HF$_2$)(3-Clpyradine)$_4$]BF$_4$

Daniel M. Pajerowski [1,*], Andrey P. Podlesnyak [1], Jacek Herbrych,[2] and Jamie Manson[3]

[1]*Neutron Scattering Division, Oak Ridge National Laboratory, Oak Ridge, Tennessee 37831, USA*

[2]*Department of Theoretical Physics, Wrocław University of Science and Technology, 50-370 Wrocław, Poland*

[3]*Department of Chemistry and Biochemistry, Eastern Washington University, Cheney, Washington 99004, USA*

[Ni(HF$_2$)(3-Clpyradine)$_4$]BF$_4$ (NBCT) is a one-dimensional, $S = 1$ spin-chain material that shows no long-range magnetic order down to thermometer temperatures of 0.1 K. Previous ambient pressure inelastic neutron scattering experiments identified NBCT to be in the large-D quantum paramagnetic phase of the D/J phase diagram, where D is the axial single-ion anisotropy and J is the intrachain superexchange. Here, we extend the previous experiments to a hydrostatic pressure of 0.9 GPa. By comparing to density matrix renormalization group calculations, we find D/J increases from 1.5 to 3.2 as pressure increases from 0 GPa to 0.9 GPa, which pushes the system further into the large-D phase.

I. INTRODUCTION

Recently, there has been a correction to the trajectory for considering and discussing states of condensed matter. Namely, it is being emphasized that classification of states by ordering and symmetry is not sufficient for some phases and instead there must be a topological classification [1]. The $S = 1$ spin chain is one of the simpler systems that is a gateway to the panoply of proposed topological states.

One spin Hamiltonian for an anisotropic $S = 1$ spin chain may be written as

$$H = J \sum_i \mathbf{S}_i \cdot \mathbf{S}_{i+1} + J' \sum_{\langle i,j \rangle} \mathbf{S}_i \cdot \mathbf{S}_j + D \sum_i \left(S_i^z \right)^2$$
$$+ E \sum_i \left[\left(S_i^x \right)^2 - \left(S_i^y \right)^2 \right], \tag{1}$$

where $\mathbf{S}_i = (S_i^x, S_i^y, S_i^z)$, $J > 0$ is the antiferromagnetic (AFM) intrachain (super)exchange energy, J' is the interchain (super)exchange energy, the $\langle i,j \rangle$ summation is between neighboring chains, D is the single-ion axial anisotropy, and E is the single-ion rhombic anisotropy. The phase diagram for D, E, and J was calculated in Ref. [2] and a portion is shown in Fig. 1. Further complexities may be included, such as anisotropic exchange in the so-called XXZ chains [3,4]. The bellwether $S = 1$ case that only considers isotropic AFM intrachain interactions has a nondegenerate gapped ground state that is called the Haldane phase [5–7]. Eventually, this Haldane phase was categorized as a symmetry-protected topological phase with short-range entanglement [8]. Application of other terms in Eq. (1) tunes the ground state away from the Haldane phase, such as for the $J' = 0$ and $E = 0$ critical easy-plane $(D/J)_C = 0.96845$ ratio [3] or the $J' = 0$ and $E =$ 0 critical easy-axis $(D/J)_C = -0.32$ ratio [4,9]. The large-D phase is a product state of $|S^z_i = 0\rangle$ sites and is topologically distinct from the Haldane phase. Therefore, moving across the quantum phase transition out of the Haldane phase as a function of D/J [or other parameters in Eq. (1)] is a topological phase transition, and there is no order parameter that changes during the phase transition.

Even before the heightened necessity of explicit topological descriptors for quantum states, the $S = 1$ anisotropic spin was the subject of extensive theoretical and experimental efforts. A summary of some experimental realization of $S = 1$ spin chains shows that most compounds are either deep in the Haldane phase $(D/J \lesssim 0.25)$ or deep in the large-D phase $(D/J \gtrsim 4)$ [11,12]. One exception is the [Ni(HF$_2$)(3-Clpyradine)$_4$]BF$_4$ (NBCT) compound that bulk measurements assigned to $D/J = 0.88$ [13]. Inelastic neutron scattering (INS) of an isotopically doped polycrystalline NBCT compound later assigned $D/J = 1.51$ and $E/J = 0.05$ [10] based upon the spin correlations that were fit to density matrix renormalization group (DMRG) calculations. The small (<0.1 meV) gap observed for NBCT is consistent with the upper limit on the critical field $(H_c \lesssim 35 \pm 10\,\text{mT})$ seen in 50-mK magnetization measurements [14].

The NBCT crystal is a coordination polymer that crystallizes in the $P2_1/c$ space group [13] (Fig. 2). The magnetic chains are identified to be along the c-axis ($c = 12.291$ Å) that has an F-H-F$^-$ spin exchange between the formally $S = 1$ Ni^{2+} magnetic ions, as seen in density functional theory calculations [13] and the INS [10]. There are two Ni^{2+} sites within the unit cell along the chain so the AFM zone center is at a momentum of $2\pi/c = 0.511$ Å^{-1}. These Ni^{2+} sites have distorted octahedral coordination spheres with F-coordination along the c-axis chain direction and N coordination in the plane of the octahedra. The spins have an easy-axis anisotropy (D > 0) with a preferential direction in the N$_4$ plane, as seen in UV-visible spectroscopy [13] and INS [10]. The pyridine
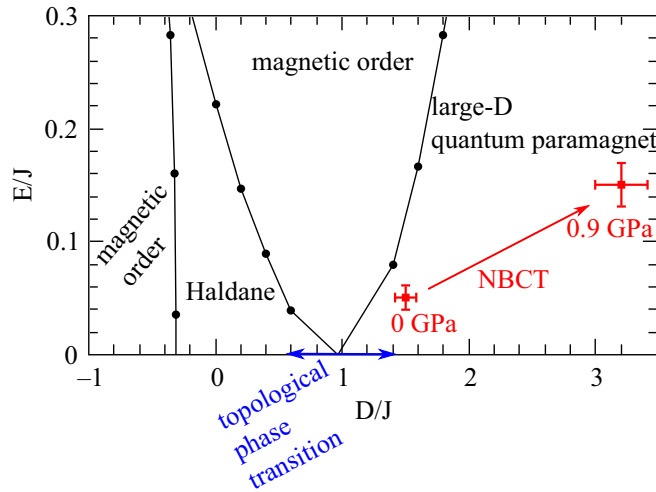
*pajerowskidm@ornl.gov

FIG. 1. Anisotropic spin-chain phase diagram. The theoretical boundary is from Ref. [2]. The point for NBCT at 0 GPa is from Ref. [10] and the 0.9-GPa point for NBCT is from this work. The uncertainty bars for NBCT data are derived from model fitting.

rings provide a large separation between the chains (e.g., $J' \ll J$), and no magnetic diffraction peaks were found down to 0.1 K [10], as well as no long-range order signatures in specific heat or muon relaxation down to 0.3 K [13]. All experimental evidence points to NBCT being described well by J, D, and E, although there has been no formal investigation of antisymmetric or anisotropic exchange, and the low symmetry of the crystal allows all three components of the antisymmetric exchange and all nine components of the exchange tensor.

This INS technique is especially diagnostic as it directly probes time and space magnetic correlations, and has been leveraged extensively for the investigation of spin chains [15]. These spin-spin correlations are observed in INS via the conjugate energy and momentum spaces. The $D = E = 0$ Haldane phase has triply degenerate lattice periodic spin-spin correlations $\langle S^\alpha S^\alpha \rangle$ (where $\alpha = x, y, z$) with the Haldane gap at the AFM zone center (often called the π-point). Numerical DMRG calculations find the Haldane phase gap at the π-point
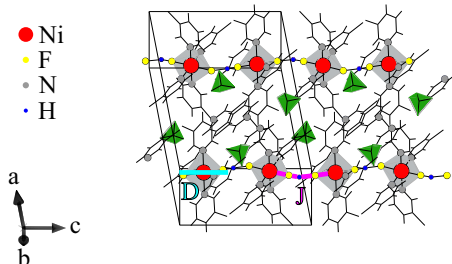
to be $\Delta = 0.41 J$ [16]. As anisotropy is increased, this gap closes and goes to zero at the $(D/J)_C$ points described earlier. The introduction of axial D anisotropy breaks the degeneracy of longitudinal $\langle S^z S^z \rangle$ and transverse $\langle S^x S^x \rangle = \langle S^y S^y \rangle$ spin-spin correlations, so two lattice periodic modes are observed in INS. The further introduction of rhombic E anisotropy separates $\langle S^x S^x \rangle$ and $\langle S^y S^y \rangle$ correlations to give three distinct modes. The effects of these anisotropies on the spin-spin correlations may be captured by DMRG calculations.

The previous INS report on NBCT placed it at a position in the (D,E)-phase space that is precipitously close to a line separating the large-D phase assignment and a Néel phase, suggesting that external pressure could modify D, E, and J, and induce a quantum phase transition. The effect of pressure for these parameters is highly specific to the material, and each term may either increase or decrease. For example, the distances and angles of the Ni-F-H-F-Ni exchange pathways of NBCT could change with pressure and modify the J parameter to either increase or decrease. Hypothetically, pressure could even tune through the Néel phase into the topologically distinct Haldane phase. The application of external pressure has previously been used with INS to show a quantum phase transition in the $S = 1/2$ dimer compound TlCuCl$_3$ [18]. An INS study of the Haldane spin chain Ni(c_2H$_8$N$_2$)$_2$NO$_2$ClO$_4$ material showed a modification of the D/J ratio from 0.16 to 0.09 as pressure increased from ambient to 2.5 GPa [19], but no change in phase was observed.

Here, the effect of 0.9 GPa of hydrostatic pressure on the spin-spin correlations of NBCT as probed by INS is presented. The experimental 0.9-GPa spectra are quantified using DMRG calculations of the dynamical spin structure factor $S(|\mathbf{Q}|, \hbar\omega)$ arising from Eq. (1), with $J' = 0$ to extract D, J, and E. Fits to the data show that pressure increases D/J from 1.5 at 0 GPa to 3.2 at 0.9 GPa and drives the system deeper into the large-D quantum paramagnetic phase. Additional technical details are given in Appendix A.

II. RESULTS AND DISCUSSION

Neutron spectra of polycrystalline NBCT were collected using a NiCrAl-alloy clamp pressure cell at $P = 0.9$ GPa, temperatures of $T = 15$ K and 0.3 K, and incident energy (Ei) values of $Ei = 12.0$ meV, 3.32 meV, 1.55 meV, and 1.00 meV. No magnetic signal was observed above sample energy gains of $\hbar\omega \approx 1.2$ meV. Reverse-powder-averaged, one-dimensional (1D) scattering functions were extracted from these powder data using the reported method [20], and the one-dimensional Brillouin zone spans $Q_{1D} = [0, 2]$. The scattering from the pressure cell is greater than the scattering from more standard aluminum cans, so $T = 15$-K data were subtracted from $T = 0.3$-K data to illustrate the spin correlations better. Representative unsubtracted data are shown in Appendix B. A gapped, lattice periodic mode is visible in the $Ei = 3.32$-meV spectra (Fig. 3). The powder data in Fig. 3(d) are reverse-powder-averaged to yield the data in Fig. 3(b). Even at $T = 15$ K, there is still inelastic scattering from the sample in the region of interest, but increasing temperature smears out the correlations, as can be seen in Fig. 5(c) of Ref. [10], and this gives rise to an oversubtraction of the background.

FIG. 2. Crystal structure of [Ni(HF$_2$)(3-Clpyridine-D_4)$_4$]^{11}BF$_4$ (NBCT). Atoms along the magnetic interaction and in the nickel coordination sphere are shown; other atom representations are suppressed, but all nearest neighbor bonds are illustrated. The green polyhedra are the BF$_4$ units and the rings of bonds are the (3-Clpyridine-D_4). Schema for the D and J parameters of Eq. (1) are shown. This figure is a modification of an output generated by VESTA [17].
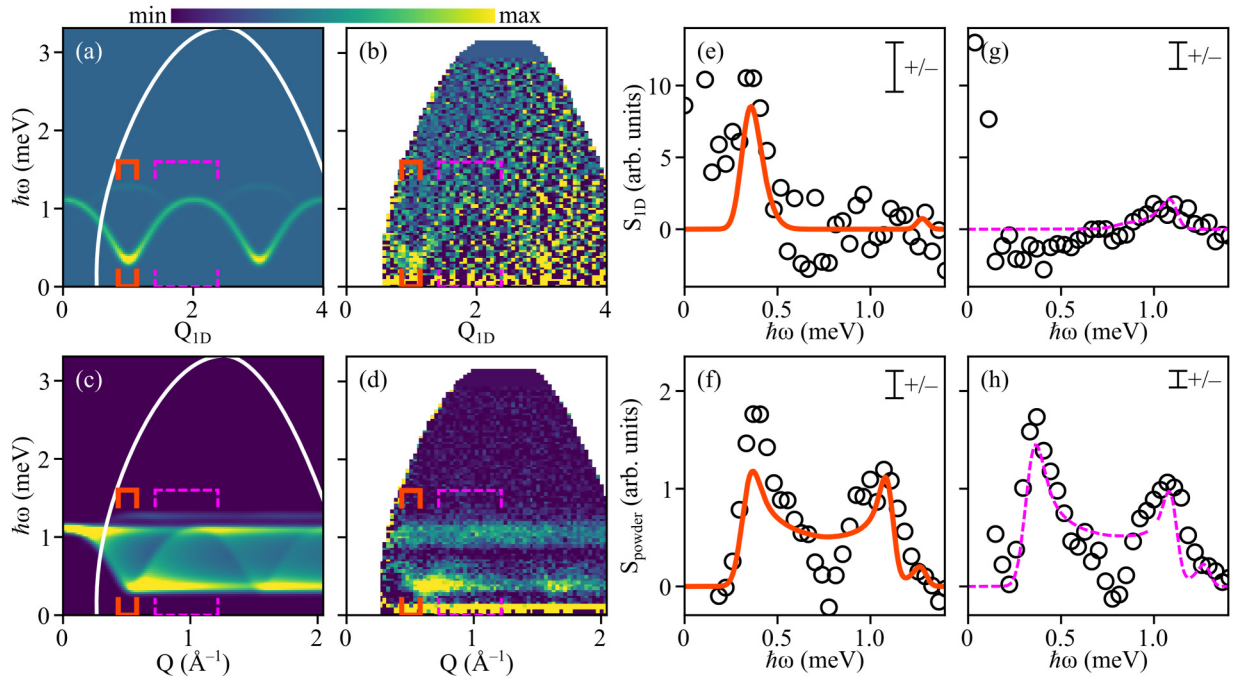
FIG. 3. $P = 0.9$ GPa, $Ei = 3.32$ meV, subtraction of $T = 15$ K from $T = 0.3$ K neutron scattering spectra. The reverse-powder-averaged (a) model and (b) data, and the powder data for (c) model and (d) data are shown. The graphed brackets illustrate the binning regions used for the scatterplots. White lines on the model show the kinematic constraint boundary, and white regions in the data are outside the kinematic constraint. Momentum integrations $Q = [0.4335, 0.5785]$ Å^{-1} that include the 1D Brillouin zone center are shown for (e) reverse-powder-averaged and (f) powder data. Momentum integrations $Q = [0.7235, 1.2165]$ Å^{-1} that include the 1D Brillouin zone boundary are shown for (g) reverse-powder-averaged and (h) powder data. The scatterplots use open circles for data and lines for the model. The uncertainty from counting statistics is given by the "$+/-$" bar.

To connect these experimental neutron scattering data to Eq. (1), the spin correlations were calculated with DMRG. A phenomenological parametrization of these spectra is possible using lattice periodic modes, with functional forms motivated by linear spin-wave theory [Eqs. (3) and (4) in Appendix A], but the resulting parameters have no built-in mapping to those in Eq. (1), and each $\langle S^\alpha S^\alpha \rangle$ mode is independent. Instead, the approach taken here is to use DMRG calculations that have D, J, and sometimes E as inputs to connect the neutron spectra to the phase diagram in Fig. 1. The DMRG spectra were themselves parameterized before comparing with the experiment to reduce numerical noise, as numerical noise can be especially problematic when powder-averaging the calculations; details are in Appendix A.

The lower resolution $Ei = 3.32$-meV data are fit with the two intrinsic parameters D and J, and one extrinsic fit parameter that scales the overall intensity. No splitting of the $\langle S^{x/y} S^{x/y} \rangle$ mode was modeled for this incident energy. Fitting the $Ei = 3.32$-meV data yields the models illustrated in Fig. 3 that use $D = 0.67$ meV and $J = 0.21$ meV (uncertainties estimated from fitting to be ± 0.01 meV). The data and model are presented as color maps to compare broadly Fig. 3(a) with Fig. 3(b), Fig. 3(c) with Fig. 3(d), and as scatterplots in Fig. 3(e)–3(h) for a more quantitative visual comparison. The integration ranges that generate S_{1D} and S_{powder} as a function of $\hbar\omega$ were chosen to emphasize a region near the AFM zone center [within 0.5060 Å$^{-1} \pm 0.0725$ Å^{-1} for Fig. 3(e) and (f)] and a region near the AFM zone boundary

[within 0.9700 Å$^{-1} \pm 0.2465$ Å^{-1} for Fig. 3(g) and 3(h)], the latter range chosen to be larger due to a weaker intensity in that region. The D anisotropy splits the triply degenerate Haldane mode into two modes, $\langle S^z S^z \rangle$ and $\langle S^{x/y} S^{x/y} \rangle$, which can be most clearly seen in the model plot of Fig. 3(a) of the dispersion along the chain. For the powder-averaged model of Fig. 3(c), the $S^z S^z$ mode is visually present mainly as a smeared line that is flat in momentum. The largest spectral weight is associated with the $\langle S^{x/y} S^{x/y} \rangle$ band that is lower in energy at the AFM zone center. The $S^z S^z$ mode is pushed higher in energy with D and has less spectral weight than $\langle S^{x/y} S^{x/y} \rangle$. The location of the $S^z S^z$ mode has an intensity consistent with the calculations [Fig. 3(f) and 3(h)] around 1.3 meV, although the intensity is close to the limit of observation. However, in the 0-GPa data [10], intensity consistent with the $S^z S^z$ mode was observed (Appendix C). The bottom of the $\langle S^{x/y} S^{x/y} \rangle$ band has a gap at the AFM zone center that increases from $\Delta_{x/y} = 0.080$ meV at 0 GPa [10] to $\Delta_{x/y} = 0.332$ meV at 0.9 GPa. The value of $\Delta_{x/y} = 0.332$ meV for $D = 0.67$ and $J = 0.21$ is in perfect agreement with the value of the gap from large-D expansion to third order in J/D [21,22]. The plots of intensity versus $\hbar\omega$ in Fig. 3(e)–3(h) show intensity below the gap that is not present in the model, but for this incident energy the resolution is sufficiently coarse that such scattering is indiscernible from the elastic line. In addition to the dispersive modes, there is also a mode that is flat in momentum peaked at $\hbar\omega = D$, similar to the observation at 0 GPa for NBCT [10]. The magnetic susceptibility of NBCT
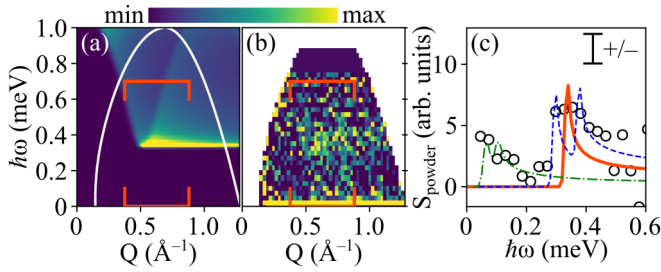
FIG. 4. $P = 0.9$ GPa, $Ei = 1.00$ meV, subtraction of $T = 15$ K from $T = 0.3$ K neutron scattering spectra. The powder data for (a) model and (b) data are shown. Brackets illustrate the binning regions used for the scatterplots. White lines on the model show the kinematic constraint boundary; white regions in the data are outside the kinematic constraint. (c) Momentum integrations $Q = [0.376, 0.880]$ Å^{-1} are shown. The scatterplots use open circles for data. There is a thick red line for the model using $D = 0.67$-meV and $J = 0.21$-meV parameters fit from $Ei = 3.32$ meV ($\Delta_E = 0$). There is a dashed blue line for the model using $D = 0.67$ meV, $J = 0.21$ meV, and adding the phenomenological $\Delta_E = 0.07$ meV. There is a thin green dotted-dashed line for the NBCT 0-GPa parameters $D = 0.53$ meV and $J = 0.35$ meV, with $\Delta_E = 0.05$ meV. The uncertainty from counting statistics is given by the "+/−" bar.

has a Curie tail component at low temperatures [13], and this nondispersive scattering is assigned to that paramagnetic species.

Measuring with lower incident energy reduces the flux and reduces the accessible momentum and energy transfers, but provides a sharper resolution. The $Ei = 1.00$-meV data show the bottom of the band to be broader than the instrumental resolution (Fig. 4). The solid red line in Fig. 4(c) is narrower than the spread of data at the gap. This broadening could be due to a distribution of D and J values due to pressure variations, but may also have a component due to the rhombic E term. For higher resolution data, an additional intrinsic parameter Δ_E captures the effect of the rhombic E term by splitting the $\Delta_{x/y}$ gap of $\langle S^{x/y} S^{x/y} \rangle$ into the two modes $\langle S^x S^x \rangle$ and $\langle S^y S^y \rangle$ as $\Delta_x = \Delta_{x/} + \Delta_E/2$ and $\Delta_y = \Delta_{x/y} - \Delta_E/2$. The splitting Δ_E may be connected to E either by calculations such as DMRG, exact diagonalization, or perturbation theory. Fitting these $Ei = 1.00$-meV data with values of D and J fixed from the $Ei = 3.32$ meV data yields a value of $\Delta_E = 0.07 \pm 0.01$ meV. This rhombic splitting is shown as the dashed blue line in Fig. 4(c). A similar fitting was performed in previous work of NBCT at 0 GPa to yield $\Delta_E = 0.05 \pm 0.01$ meV, which was modeled to extract $E/J = 0.05$, with $J = 0.35$ meV and E = 0.018 meV [10]. If the width of the $\Delta_{x/y}$ mode is solely due to rhombic splitting, then E may be estimated from Δ_E using exact diagonalization of a ring of eight $S = 1$ spins, with $D = 0.67$ and $J = 0.21$. For E = 0, the exact diagonalization yields $\Delta_{x/y} = 0.325$ meV. For the E/J values from 0 to 0.25, a linear dependence of $\Delta_E = 0.4731 \times E/J$ was found, which yields $E/J = 0.15 \pm 0.02$ (E = 0.032 ± 0.004 meV) for NBCT at 0.9 GPa. Uncertainties are standard deviations of the fitting parameters.

These $Ei = 1.00$-meV data also show that there is finite intensity below the gap of the $\langle S^{x/y} S^{x/y} \rangle$ band. The source of this additional intensity could be due to multiple scattering,
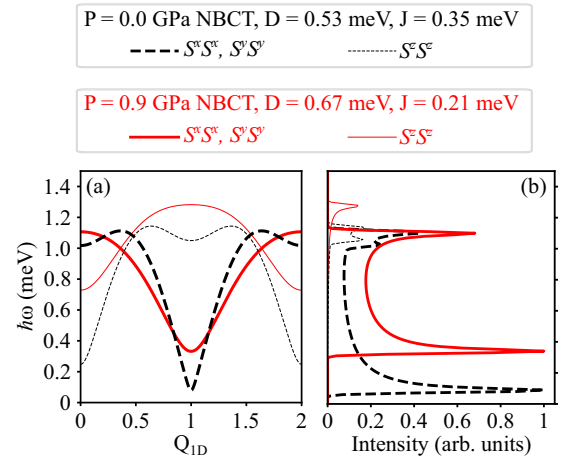

FIG. 5. Pressure induced changes to model (a) dispersion along the chain and (b) spectral weight integrated in the 1D Brillouin zone.

quasi-elastic scattering, or perhaps from a region in the sample that did not wet with the pressure medium and remained at nominally zero pressure. The statistics are not enough to make a definitive statement about the source of this intensity in the gap, although the data are suggestive that this extra scattering has an intrinsic component, as it is larger at the AFM zone center. If $\approx 10\%$ of the sample were at nominally zero pressure, this extra intensity is reproduced as illustrated with the dotted-dashed green line in Fig. 4(c) that could be added to the high-pressure dashed blue line to reproduce the intensities in those data. All DMRG calculations are for zero temperature, so it could be that this scattering is a thermal effect, although for $T = 0.3$ K there is less than 0.001% population in a 0.3-meV state above the ground state. This intensity in the gap is also present in the $Ei = 1.55$-meV data (Appendix D).

At zero pressure, NBCT was previously identified to be precipitously close to a quantum phase transition from the large-D phase to either the Haldane phase or a Néel phase, and it was hypothesized that pressure could be used to drive the system critical [10]. These high-pressure neutron-scattering data of NBCT show the gap to open up with pressure, and model fits show the system to be driven away from a quantum phase transition and, instead, deeper in the large-D phase (Fig. 1). There is no model from Eq. (1) within the Haldane phase that accurately describes the features of these 0.9-GPa NBCT data. The effect of pressure on NBCT is illustrated with the dispersions of the $S^z S^z$ and $\langle S^{x/y} S^{x/y} \rangle$ modes in Fig. 5, where the spectral weights have been normalized to the peak intensity. The rhombic E term (or phenomenologically Δ_E) would modify these plots by splitting $\langle S^{x/y} S^{x/y} \rangle$. The modifications to the spin correlations with pressure are striking, considering the modest pressure of 0.9 GPa. These pressure-induced changes suggest that a material similar to NBCT may be designed that could have a pressure-induced quantum phase transition. However, our result shows that for NBCT, a negative pressure either via doping or some mechanical strain is required in order to induce a quantum phase transition. Single-crystal data would also be helpful to refine these powder-based models, potentially including other terms such as antisymmetric or anisotropic exchange. It will also be

interesting to see how these INS-determined parameters for NBCT can reproduce bulk measurements such as magnetization and specific heat.

III. CONCLUSIONS

In conclusion, drastic changes in the spin-spin correlations of the anisotropic $S = 1$ spin chain [Ni(HF$_2$)(3-Clpyradine)$_4$]BF$_4$ under applied hydrostatic pressure of 0.9 GPa were observed using inelastic neutron scattering. The anisotropy increases with pressure and the exchange decreases with pressure, driving from $D/J = 1.5$ to $D/J = 3.2$ and pushing the system deeper into the large-D, with less substantial changes to E. This finding shows the large tunability of this class of coordination polymers and suggests a continued avenue of investigation for a pressure-induced topological phase transition.

The Department of Energy will provide public access to these results of federally sponsored research in accordance with the Department of Energy (DOE) Public Access Plan [23].

APPENDIX A: TECHNICAL DETAILS

A ≈ 0.1-gram portion of the same isotopically enriched polycrystalline samples as for the ambient pressure experiment [10] was mounted in the pressure cell and wet with Fluorinert^{TM} as a pressure medium. The pressure was determined at room temperature with Raman fluorescence, and this setup has shown no significant changes of pressure between ambient temperature and low temperature [25]. Cryogenic temperatures were achieved with a wet ^{3}He cryostat for the T = 0.3-K and $T = 15$-K data. The Cold Neutron Chopper Spectrometer (CNCS) at the Spallation Neutron Source was used in high-flux mode [26]. Experimental energy resolutions are from Mantid, and at $\hbar\omega = 0$ the full-width-half-max resolution of 0.02 meV, 0.04 meV, and 0.11 meV for 1-meV, 1.55-meV, and 3.32-meV incident energies, respectively [27]. The momentum resolution is modeled as a gaussian from fitting a Bragg peak for each incident energy condition. The data were normalized to the proton current on target during collection. The detectors were normalized using a vanadium standard measurement that is defined to have an average intensity per pixel of one scaled unit. Intensities are multiplied by the ratio of incident and final momentum to result in numbers that are proportional to a correlation function. All numerical optimizations used the libraries of SciPy [28].

The many-body ground state of the system is studied via the density matrix renormalization group (DMRG) method within the single-center site approach. [29–31] The dynamical correlation functions were calculated with the dynamical-DMRG method, [32,33], evaluated directly in terms of frequency via the Krylov decomposition [34]. The zero-temperature dynamical spin structure factor $S(q_{1D}, \omega)$ is evaluated as the resolvent,

$$S(q_{1D},\ \omega) = -\frac{1}{L\pi} \sum_\ell e^{i\ell q} \mathrm{Im} \langle \mathrm{gs}|S_\ell \frac{1}{\omega^+ - H + \epsilon_{\mathrm{gs}}} S_{L/2}|\mathrm{gs}\rangle,$$

$$\tag{2}$$

with $\omega = \omega + i\eta$, and $|\mathrm{gs}\rangle(\varepsilon_{\mathrm{gs}})$ as the ground-state wave vector (energy). Calculations were performed for $D/J = [3.0, 3.5, 4.0]$ using $L = 80$ sites on a chain with open-boundary conditions. Throughout the DMRG procedure, $M \approx 1200$ states are kept and ≈ 20 full sweeps are performed in the finite-size algorithm, maintaining the truncation error less than 10^{-7}. We have chosen $\delta\omega = 0.02$ as the frequency resolution with broadening $\eta = 2\omega$.
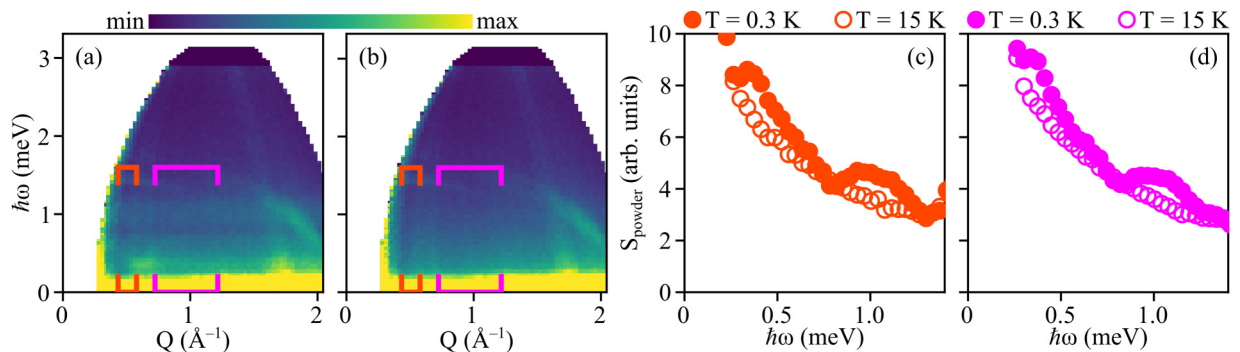

FIG. 6. $P = 0.9$ GPa, $Ei = 3.32$ meV, unsubtracted data. (a) T = 0.3-K and (b) $T = 15$-K neutron scattering spectra are shown. Momentum integrations of (c) $Q = [0.4335, 0.5785]$ Å^{-1} and (d) $Q = [0.7235, 1.2165]$ Å^{-1}.
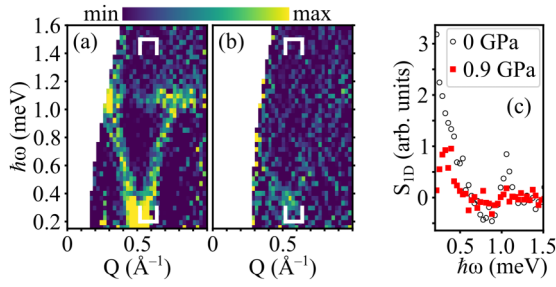
FIG. 7. Comparison of $Ei = 3.32$-meV data showing $\langle S^z S^z \rangle$ contributions. These (a) 0-GPa and (b) 0.9-GPa data are subtractions of low-temperature minus high-temperature data visualized as a reverse-powder average. Brackets illustrate the binning regions, $Q = [0.52, 0.64]$ Å^{-1}, used for (c) the scatterplot.

For denoising, these DMRG correlations were fit to the same phenomenological relationships used in the ambient pressure study of NBCT,

$$I(q_{1D}, \hbar\omega) = [1 - \cos(q_{1D})]\left(I_0 + \frac{I_{-1}}{\hbar\omega}\right) \quad (3)$$

and

$$\frac{E(q_{1D})}{J} = \sqrt{A \cos\left(\frac{q_{1D}}{2}\right)^2 + v^2 \sin^2(q_{1D}) + \Delta^2}, \quad (4)$$

where the dispersion relationship parametrization is inspired by linear spin-wave theory [35]. The resulting parameters

were then interpolated with cubic splines to give smooth functions of A, V, Δ, I_0, and L_1 for the $\langle S^x S^x \rangle$, $\langle S^y S^y \rangle$, and $\langle S^z S^z \rangle$ correlation functions. The $\langle S^{x/y} S^{x/y} \rangle$ correlations were further split by letting $\Delta_{x/y} \rightarrow \Delta_{x/y} \pm \Delta_E/2$. The validity of the Δ_E Δ_E parametrization to capture the resulting correlation was checked with DMRG and found to be satisfactory. To compare DMRG with the experiment, a Bose factor was included to modify the intensity as a function of $\hbar\omega$. The Ni^{2+} magnetic form factor was included to modify the intensity as a function of momentum transfer [36].

APPENDIX B: UNSUBTRACTED DATA WITH PRESSURE CELL CONTRIBUTION

These high-pressure measurements are experimentally more challenging due to the smaller sample volumes and larger scattering from the containment. Neutron scattering events associated with the pressure cell and with multiple scattering from the sample position to the surrounding equipment are visible in the unsubtracted data for $Ei = 3.32$ meV (Fig. 6). Unlike the signal from the sample, these extrinsic scattering features are essentially independent of temperature for the ranges investigated. Even on top of the large background contributions, the essential features of the data are visible in the one-dimensional integrations [Fig. 6(c) and Fig. 6(d)]. There is the intensity from the bottom of the dominant mode, the intensity at the top of the mode, and the flat mode we associate with single-ion-like excitations.
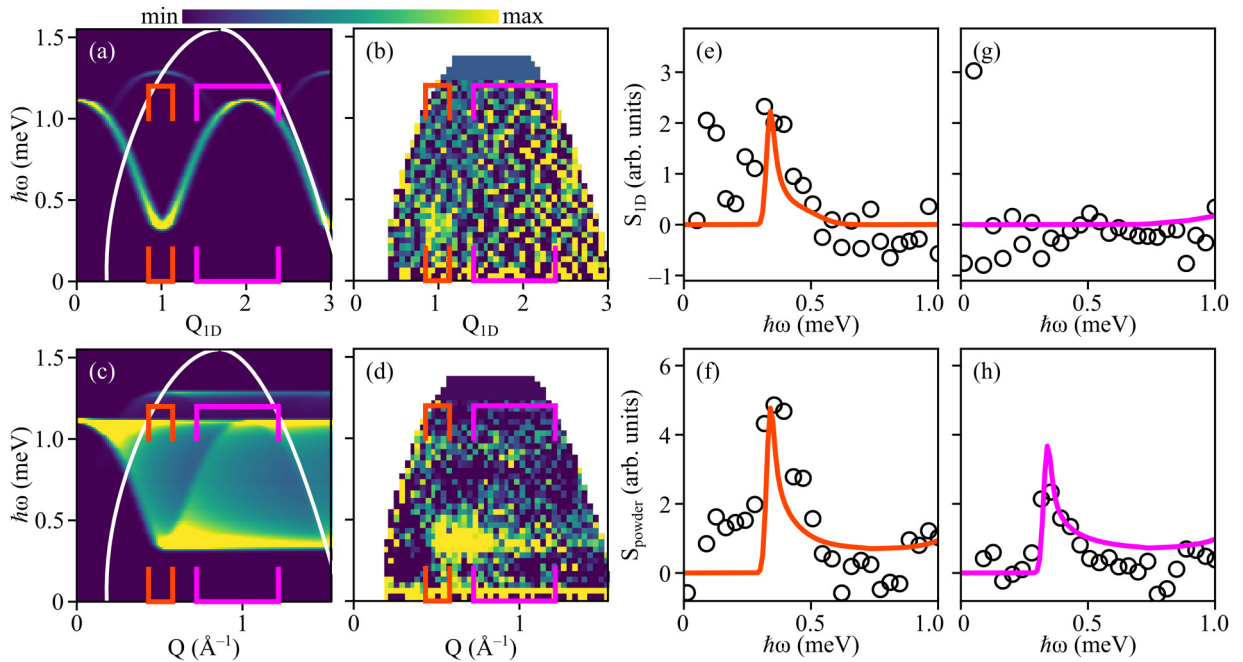

FIG. 8. $P = 0.9$ GPa, $Ei = 1.55$ meV, subtraction of $T = 15$-K from $T = 0.3$-K neutron scattering spectra. The reverse-powder-averaged (a) model and (b) data, and the powder data for (c) model and (d) data are shown. Brackets illustrate the binning regions used for the scatterplots. White lines on the model show the kinematic constraint boundary; white regions in the data are outside the kinematic constraint. Momentum integrations $Q = [0.468, 0.628]$ Å^{-1} are shown for (e) reverse-powder-averaged and (f) powder data. Momentum integrations $Q = [0.788, 1.332]$ Å^{-1} are shown for (g) reverse-powder-averaged and (h) powder data. The scatterplots use open circles for data and lines for the model.

APPENDIX C: $\langle S^z S^z \rangle$ MODE IN 0 GPa VERSUS 0.9 GPa

A combination of effects make observation of the $\langle S^z S^z \rangle$ mode for the high-pressure 0.9 GPa difficult. The available sample volume of the pressure cell is less than a standard can, and the extra material required to achieve high pressures decreases the transmission and increases the background scattering. Conversely, the reverse-powder-averaged 0-GPa NBCT data [10] do show scattering consistent with an $\langle S^z S^z \rangle$ mode (Fig. 7).

APPENDIX D: $Ei = 1.55 \, \text{meV}$

Data were also collected for $Ei = 1.55 \, \text{meV}$ (Fig. 8). These data are consistent with and further support the findings in the main body for $Ei = 3.32 \, \text{meV}$ and $Ei = 1.00 \, \text{meV}$.

[1] X. G. Wen, Rev. Mod. Phys. **89**, 041004 (2017).

[2] Y. C. Tzeng, H. Onishi, T. Okubo, and Y. J. Kao, Phys. Rev. B **96**, 060404(R) (2017).

[3] S. Hu, B. Normand, X. Wang, and L. Yu, Phys. Rev. B **84**, 220402(R) (2011).

[4] W. Chen, K. Hida, and B. C. Sanctuary, Phys. Rev. B **67**, 104401 (2003).

[5] F. D. M. Haldane, Phys. Rev. Lett. **50**, 1153 (1983).

[6] F. D. M. Haldane, Phys. Lett. A **93**, 464 (1983).

[7] F. D. M. Haldane, Rev. Mod. Phys. **89**, 040502 (2017).

[8] Z. C. Gu and X. G. Wen, Phys. Rev. B **80**, 155131 (2009).

[9] A. F. Albuquerque, C. J. Hamer, and J. Oitmaa, Phys. Rev. B **79**, 054412 (2009).

[10] D. M. Pajerowski, J. L. Manson, J. Herbrych, J. Bendix, A. P. Podlesnyak, J. M. Cain, and M. W. Meisel, Phys. Rev. B **101**, 094431 (2020).

[11] K. Wierschem and P. Sengupta, Mod. Phys. Lett. B **28**, 1430017 (2014).

[12] O. V. Maximova, S. V. Streltsov, and A. N. Vasiliev, Crit. Rev. Solid State Mater. Sci. **46**, 371 (2021).

[13] J. L. Manson, A. G. Baldwin, B. L. Scott, J. Bendix, R. E. Del Sesto, P. A. Goddard, Y. Kohama, H. E. Tran, S. Ghannadzadeh, J. Singleton, T. Lancaster, J. S. Möller, S. J. Blundell, F. L. Pratt, V. S. Zapf, J. Kang, C. Lee, M. H. Whangbo, and C. Baines, Inorg. Chem. **51**, 7520 (2012).

[14] J. S. Xia, A. Ozarowski, P. M. Spurgeon, A. G. Graham, J. L. Manson, and M. W. Meisel, J. Phys. Conf. Ser. **969**, 012121 (2018).

[15] C. Broholm, G. Aeppli, Y. Chen, D. C. Dender, M. Enderle, P. R. Hammar, Z. Honda, K. Katsumata, C. P. Landee, M. Oshikawa, L. P. Regnault, D. H. Reich, S. M. Shapiro, M. Sieling, M. B. Stone, M. M. Turnbull, I. Zaliznyak, and A. Zheludev, *High Magnetic Fields* (Springer, New York, 2002).

[16] S. R. White and D. A. Huse, Phys. Rev. B **48**, 3844 (1993).

[17] K. Momma and F. Izumi, J. Appl. Crystallogr. **44**, 1272 (2011).

[18] C. Rüegg, A. Furrer, D. Sheptyakov, T. Strässle, K. W. Krämer, H. U. Güdel, and L. Mélési, Phys. Rev. Lett. **93**, 257201 (2004).

[19] I. A. Zaliznyak, D. Dender, C. Broholm, and D. H. Reich, Phys. Rev. B **57**, 5200 (1998).

[20] K. Tomiyasu, M. Fujita, A. I. Kolesnikov, R. I. Bewley, M. J. Bull, and S. M. Bennington, Appl. Phys. Lett. **94**, 3 (2009).

[21] N. Papanicolaou, A. Orendáčová, and M. Orendáč, Phys. Rev. B **56**, 8786 (1997).

[22] C. Psaroudaki, J. Herbrych, J. Karadamoglou, P. Prelovšek, X. Zotos, and N. Papanicolaou, Phys. Rev. B **89**, 224418 (2014).

[23] http://energy.gov/downloads/doe-public-access-plan.

[24] DMRG++, https://G1257.Github.Io/DmrgPlusPlus.

[25] A. Podlesnyak, M. Loguillo, G. M. Rucker, B. Haberl, R. Boehler, G. Ehlers, L. L. Daemen, D. Armitage, M. D. Frontzek, and M. Lumsden, High Press. Res. **38**, 482 (2018).

[26] G. Ehlers, A. A. Podlesnyak, J. L. Niedziela, E. B. Iverson, and P. E. Sokol, Rev. Sci. Instrum. **82**, 085108 (2011).

[27] O. Arnold *et al.*, Nucl. Instruments Methods Phys. Res. Sect. A Accel. Spectrometers, Detect. Assoc. Equip. **764**, 156 (2014).

[28] E. Jones, T. Oliphant, and P. Peterson, SciPy Open Source Sci. Tools Python (2001).

[29] U. Schollwöck, Rev. Mod. Phys. **77**, 259 (2005).

[30] S. R. White, Phys. Rev. B **72**, 180403(R) (2005).

[31] G. Alvarez, Comput. Phys. Commun. **180**, 1572 (2009).

[32] E. Jeckelmann, Phys. Rev. B **66**, 045114 (2002).

[33] T. D. Kühner and S. R. White, Phys. Rev. B **60**, 335 (1999).

[34] A. Nocera and G. Alvarez, Phys. Rev. E **94**, 053308 (2016).

[35] S. Ma, C. Broholm, D. H. Reich, B. J. Sternlieb, and R. W. Erwin, Phys. Rev. Lett. **69**, 3571 (1992).

[36] H. Börner, J. Brown, C. J. Carlile, R. Cubitt, R. Currat, A. J. Dianoux, B. Farago, A. W. Hewat, J. Kulda, E. Lelièvre-Berna, G. J. McIntyre, S. A. Mason, R. P. May, A. Oed, J. R. Stewart, F. Tasset, J. Tribolet, I. Anderson, and D. W. Dubbers, *Neutron Data Booklet* (Old City Publishing, Philadelphia, PA, 2003).